remote sensing

MDPI

Article

Multitemporal Analysis of Observed Flood Recurrence in an Andean–Amazonian Valley in Peru: An Integration of Field Data, SAR Images, and Cloud Computing

Wilian H. Vargas-Farfan [1,2], Abner S. Rivera-Fernandez [1,3], Jhon A. Zabaleta-Santisteban [1], Angel J. Medina-Medina [1,3], Martha R. Pacheco-Huamani [1,2], Katerin M. Tuesta-Trauco [1], Alexander Cotrina-Sanchez [1], Swati Suman [4], Teodoro B. Silva-Melendez [1] and Elgar Barboza [1,3,*]

[1] Instituto de Investigación para el Desarrollo Sustentable de Ceja de Selva (INDES-CES), Universidad Nacional Toribio Rodríguez de Mendoza de Amazonas, Chachapoyas 01001, Peru; 2021205022@unam.edu.pe (W.H.V.-F.); 74305628m2@untrm.edu.pe (A.S.R.-F.); jhon.zabaleta.epg@untrm.edu.pe (J.A.Z.-S.); angel.medina@untrm.edu.pe (A.J.M.-M.); 2021205045@unam.edu.pe (M.R.P.-H.); katerin.tuesta.epg@untrm.edu.pe (K.M.T.-T.); alexander.cotrina@untrm.edu.pe (A.C.-S.); 7680096361@untrm.edu.pe (T.B.S.-M.)

[2] Grupo de Investigación en Ciencia de la Información Geoespacial, Escuela Profesional de Ingeniería Ambiental, Universidad Nacional de Moquegua, Pacocha 18610, Peru

[3] Facultad de Ingeniería Ambiental, Biosistemas y de la Energía (FIABE), Universidad Nacional Toribio Rodríguez de Mendoza de Amazonas, Chachapoyas 01001, Peru

[4] Appalachian Laboratory, Center for Environmental Science, University of Maryland, Frostburg, MD 21532, USA; swati.suman@umces.edu

* Correspondence: elgar.barboza@untrm.edu.pe; Tel.: +51-985-413-568

Highlights

What are the main findings?

- VH showed the lowest Otsu threshold dispersion among the eight retained events—a result that partly reflects VH-based event selection—and the highest accuracy point estimates in the E13 reference sample.
- The area detected as flooded at least once covered 9842.02 ha; high and very high observed recurrence accounted for 6.29%, concentrated near the Utcubamba–Marañón confluence and northern valley meanders.

What are the implications of the main findings?

- Integrating event-specific detections, observed recurrence, and land-cover information identifies repeatedly detected sectors and their agricultural exposure.
- The maps provide complementary information for territorial planning within the temporal coverage and spatial constraints of the study.

Check for updates

Academic Editors: Azad Hossain, Xiaobo Chao and Taufique Mahmood

Received: 25 August 2026
Revised: 25 October 2026
Accepted: 27 October 2026
Published: 31 October 2026

Copyright: © 2026 by the authors. Licensee MDPI, Basel, Switzerland. This article is an open access article distributed under the terms and conditions of the Creative Commons Attribution (CC BY) license.

Abstract

Flood monitoring in Andean–Amazonian valleys is constrained by sparse hydrological records and persistent cloud cover. This study mapped observed flood recurrence in the Utcubamba River Valley, Peru, during 2019–2025 using Sentinel-1 imagery processed in Google Earth Engine. PRE–POST backscatter differences were classified using Otsu thresholding and spatial constraints, including a maximum slope of 5° and a 1000 m hydrographic buffer. Eight of 13 cataloged events were retained. VH thresholds had a mean ± standard deviation of −2.83 ± 0.05 dB, compared with −1.73 ± 1.11 dB for VV and −3.33 ± 1.44 dB for $(VH+VV)^2$; the low VH dispersion is a property of the retained subset, which was selected partly on VH threshold behavior. The eight-event map covered 9842.02 ha detected as flooded at least once, with 6.29% classified as high or very high observed recurrence, concentrated near the Utcubamba–Marañón confluence. For E13, assessment against a

balanced sample of 1360 reference points yielded a sample-based overall accuracy of 85.15%, flooded-class user's accuracy of 91.64%, producer's accuracy of 77.35%, and F1 score of 0.839. These metrics characterize the sampled sectors of E13. Agricultural classes accounted for 73.70% of the area in the 2024 land-cover overlay. Irrigation-related changes could not be fully distinguished from river flooding. The resulting count of detections across cataloged events provides complementary information for land-use planning, with interpretation bounded by temporal coverage, event selection, and reference-data availability.

Keywords: observed flood recurrence; Andean–Amazonian valleys; Otsu threshold; VH polarization; Land Use and Land Cover (LULC); Utcubamba

1. Introduction

Floods are among the most frequent and destructive natural hazards worldwide, causing significant economic, social, and ecological impacts [1,2]. This threat is gradually intensifying because climate change is expected to increase the frequency and intensity of extreme weather events, including floods [3]. In Peru, flood occurrence is strongly influenced by the El Niño–Southern Oscillation (ENSO), although its effects vary according to the spatial configuration of sea-surface temperature anomalies in the tropical Pacific. Different ENSO types produce contrasting rainfall responses across Peru, with eastern-Pacific warming particularly associated with enhanced austral-summer precipitation in northern Peru, whereas other ENSO configurations can produce markedly different hydroclimatic responses over the Andes and Amazon basin [4,5]. These contrasts have contributed to recurrent high-impact flood episodes, including the severe 1982–1983, 1997–1998, and 2017 events along the northern Peruvian coast, with the 2017 Coastal El Niño producing extensive river flooding and substantial socioeconomic impacts [6]. The process is especially critical in mountainous regions, where rugged terrain limits space for development and leads to uncontrolled encroachment on highly vulnerable floodplains [7]. Because flood risk arises from the complex interaction between natural and human factors, its scientific assessment is essential for reducing losses and strengthening territorial resilience [8].

Synthetic aperture radar (SAR) sensors operate in the microwave range and acquire observations during both day and night, including under cloud cover. In addition, open water surfaces predominantly produce specular reflection and exhibit low backscatter values, making them easier to distinguish from other land covers [9,10]. Over the past decade, the increasing availability of freely accessible SAR data has expanded its use in flood mapping [9]. Cloud computing platforms such as Google Earth Engine (GEE) facilitate the processing of large Sentinel-1 datasets without extensive local computing resources, supporting multitemporal analysis at regional scales [11]. However, SAR-based monitoring still has significant limitations in vegetated and urban areas, where complex scattering mechanisms make it difficult to delineate flooded areas accurately [9,10].

Among the methodologies for delineating flooded regions using SAR, change detection is particularly prominent. This technique compares backscatter data acquired before and after an event to identify reductions indicative of water presence [12]. Regarding difference images, Otsu's automatic thresholding technique has been widely utilized to determine a classification threshold by maximizing interclass variance, without the need for training data. This method has been effectively employed across diverse contexts, including monitoring seasonal tropical wetlands such as the Pantanal [13], evaluating damage to rice paddies caused by tropical storms [14], and integrated time-series frameworks on cloud platforms [11,15]. However, the method's effectiveness decreases in large images

where water constitutes a minor portion of the overall area, making it difficult to identify the bimodal histogram distribution on which the threshold relies [16]. In topographically complex environments, integrating data from digital elevation models helps restrict analysis to regions with gentle slopes where water response is consistent, improving classification accuracy [17,18]. In this way, multiple combinations of polarization have been evaluated to optimize discrimination: VH cross-polarization has demonstrated greater potential than VV for mapping flooded crops [19], while the combination $(VH + VV)^2$ calculated on a linear scale can improve the separability between flooded and non-flooded areas compared to the use of individual polarizations [16,20].

Beyond mapping individual events, multitemporal analysis of SAR time series helps characterize the spatial distribution of repeated flood detections [21]. Systematic processing of Sentinel-1 time series can also support the reconstruction of historical inundation patterns [22,23]. Integrating these maps with Land Use and Land Cover (LULC) information substantially increases their operational value by enabling an assessment of the differential exposure of agricultural systems, urban areas, and natural ecosystems to flooding [24]. In this context, geospatial approaches applied to risk zoning have shown that the areas of greatest danger are concentrated near river channels and in developed areas, where unplanned development increases impervious surfaces and alters natural water flows [24]. Therefore, generating flood recurrence maps through multitemporal analysis provides relevant information for land-use planning and regulation and the design of mitigation strategies [23].

Steep-sided Andean valleys present complex geomorphological conditions that influence the interpretation of radar observations through effects such as shadowing and layover [18,25]. These challenges are typical of SAR monitoring in regions with complex topography and underscore the increasing necessity for methodologies tailored to such environments [18,25]. Despite this limitation, a prevalent approach involves limiting analysis to low-slope regions where the water response remains physically consistent. Restricting the analysis to low-slope terrain focuses mapping on the floodplain, where agricultural land and settlements are concentrated, although it does not correct terrain-related distortions in SAR observations. However, studies that integrate multitemporal SAR analysis with the creation of historical recurrence maps and their validation through fieldwork are notably scarce in mountainous environments with limited hydrological and topographic data. Such rigorous quantitative assessments using high-quality reference data are essential for the reliability of these products [9,26]. This deficiency is particularly pronounced in the Utcubamba River valley, one of the principal tributaries of the Marañón River in Peru's Amazonas Department, where limited research has been conducted in the past regarding the multitemporal dynamics of flooding using Sentinel-1 images processed in GEE.

Although automatic thresholding approaches using Sentinel-1 imagery and cloud-computing platforms have demonstrated considerable potential for flood mapping, multitemporal applications focused on flood recurrence remain comparatively limited in Peruvian Andean–Amazonian valleys. Optical observations are frequently constrained during flood events by cloud contamination, whereas SAR imagery provides observations under cloud cover suitable for event-based and multitemporal monitoring [27]. Consequently, the integration of automatic SAR-based flood detection, observed recurrence mapping, accuracy assessment, and geomorphological characterization remains insufficiently explored in this geographical context. In this context, the aim of this study was to map the observed recurrence of flooding in the Utcubamba River Valley among officially cataloged events during 2019–2025 using Sentinel-1 SAR imagery, and to characterize the land cover exposed within the detected areas. In this study, flood detection

refers to the area classified as flooded in each event; observed recurrence is the number of retained cataloged events in which a pixel was detected as flooded, rather than a hydrological flood frequency or return period; and exposure denotes the land-cover classes located within the detected areas [28]. Flood probability, vulnerability, and risk were not estimated. Flooded areas were delineated using backscatter change detection combined with topographically constrained automatic Otsu thresholding. An observed flood recurrence map was subsequently generated from the retained events identified during the study period. The relationship between detected areas and LULC classes was also assessed. Classification accuracy was evaluated for E13 using reference data derived from Sentinel-2 imagery, while official event records and UAV-based field surveys provided documentary and geomorphological context. This study therefore provides an event-based characterization of repeated flood detections in the Utcubamba Valley and a comparison of SAR variables for threshold-based detection in an intensively cultivated Andean landscape, supporting the use of SAR-derived flood products in data-scarce Andean environments.

2. Materials and Methods

2.1. Study Area

The study area comprises the Utcubamba River Valley, located in the department of Amazonas in northern Peru (Figure 1). The valley covers approximately 744.24 km^2 and ranges in elevation from 349 to 800 m above sea level. Geographically, it extends between the provinces of Utcubamba and Bagua, with the Utcubamba River serving as the main hydrological axis and flowing through the valley from south to north until it joins the Marañón River.

The Utcubamba River originates in the district of Leymebamba (province of Chachapoyas) at approximately 3100 m above sea level and flows about 253 km in a south-to-north direction until it joins the Marañón River, draining a watershed of approximately 6400 km^2, which represents about 15% of the territory of the Amazonas Department [29]. The valley bottom, where the studied floodplain is located, lies within the Marañón Seasonally Dry Tropical Forest ecoregion, characterized by a warm, semiarid climate with average temperatures of 24–25 °C and marked seasonal variation in precipitation, which ranges approximately from 600 to 1300 mm depending on the altitudinal zone and is concentrated mainly during the first half of the year [30,31].

The main wet and flood season generally extends from December to April [32]. Three retained events occurred outside this period: E04 in October, E06 in June, and E08 in November. Their documentary context is considered separately from the interpretation of individual SAR detections. Hydrological modeling for the Utcubamba basin has projected increases of up to 14.80% in peak discharge under the SSP5-8.5 scenario [33], providing further motivation for documenting historical flood patterns.

The lower Utcubamba floodplain, particularly the districts of Bagua Grande and Cajaruro, is an important rice-producing area. Agriculture accounted for 29.40% of regional gross value added in 2024, while paddy rice represented 33.20% of agricultural production and reached 330.1 thousand metric tons [34]. The 2017 census recorded 107,237 inhabitants in Utcubamba Province [35]. The city of Bagua Grande also serves as a major transportation center between the coast and the Amazon region, concentrating population, infrastructure, and economic activities in areas near the valley's floodplain.

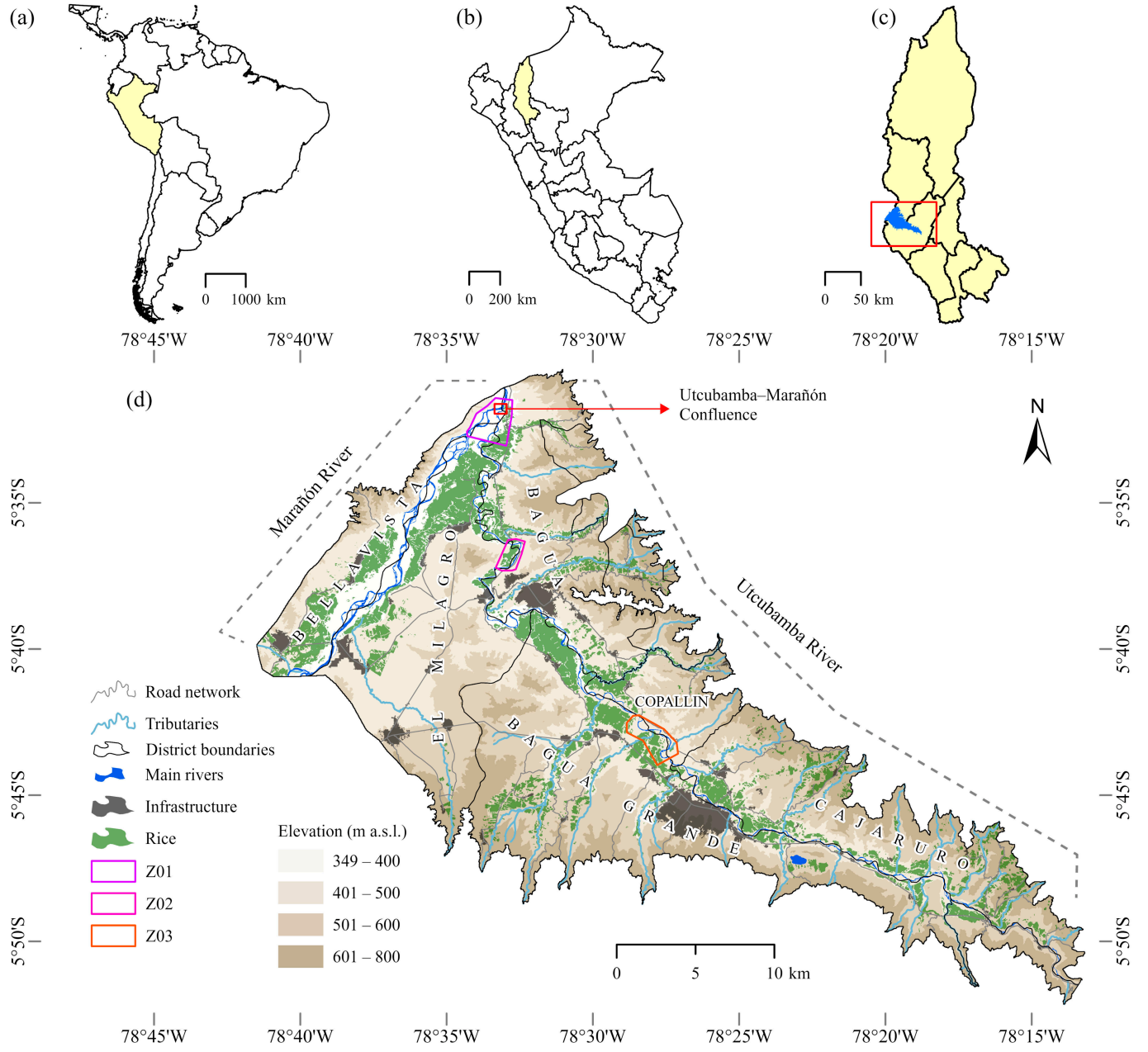


Figure 1. Location of the study area: (**a**) Peru in South America, (**b**) Amazonas in Peru, (**c**) Study area in Amazonas, (**d**) Utcubamba Valley, showing the Utcubamba–Marañón confluence, the UAV survey zones (Z01–Z03, referred to as Zones 1–3), and district boundaries. Data sources: Copernicus GLO-30 DEM, MapBiomas Peru Collection 3, and Sentinel-2. Coordinate reference system: WGS 84 (EPSG:4326).

2.2. Methodological Framework

The methodology integrated multitemporal analysis of SAR imagery, cloud-based geospatial processing, and topographic criteria to detect and characterize floods in the Utcubamba River Valley. The workflow comprises six steps: (i) SAR preprocessing, (ii) flood detection based on backscatter changes, (iii) spatial filtering, (iv) event quality control, (v) multitemporal recurrence analysis, and (vi) accuracy assessment, geomorphological characterization, and exposure analysis. Figure 2 groups these steps into five panels and a lower branch: panel (a) shows the input data; panels (b) and (c) cover steps (i)–(iii); panel (d) corresponds to step (v); panel (e) shows the exposure analysis; and

the lower branch shows event quality control, the accuracy assessment of E13, and the geomorphological context.

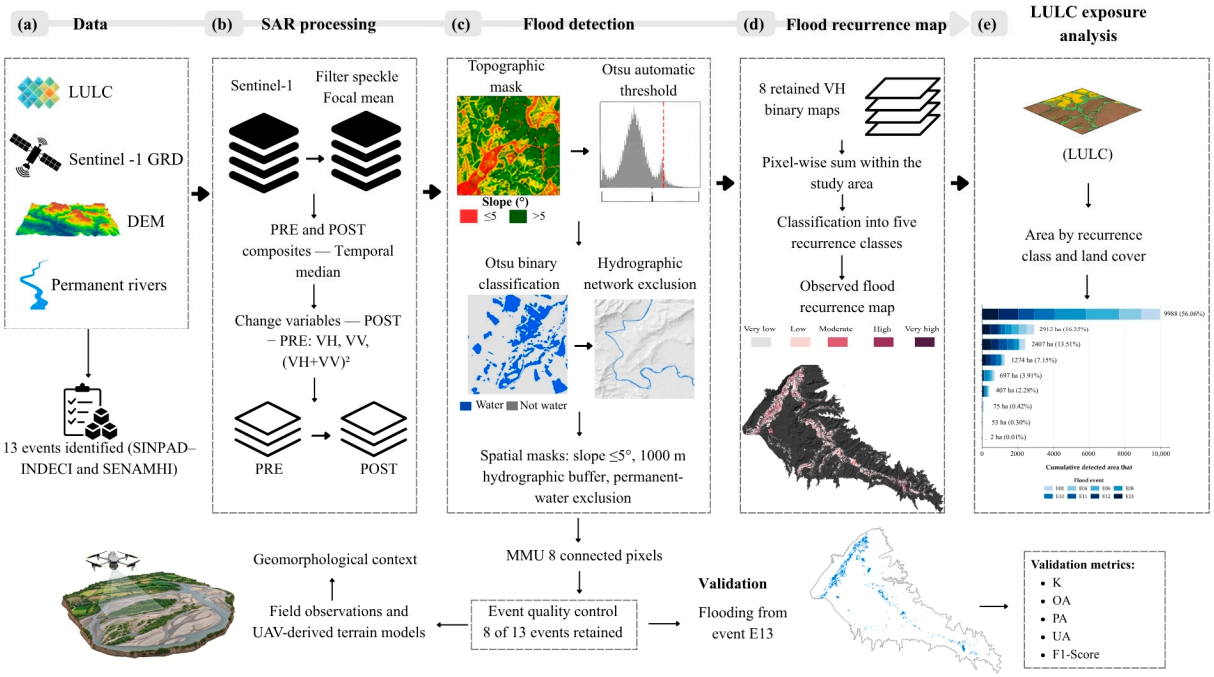


Figure 2. Methodological workflow. Panels: (**a**) input data, (**b**) SAR processing, (**c**) flood detection, (**d**) observed flood recurrence map, and (**e**) LULC exposure analysis. The lower branch shows event quality control (8 of 13 events retained), the accuracy assessment of the reference event (E13), and the geomorphological context from field observations and UAV-derived terrain models.

2.3. Delimitation of the Study Area

The study area was delineated in ArcGIS Pro 3.5.4 by reclassifying a Digital Elevation Model (DEM) [36], using an elevation threshold of 800 m above sea level. This delineation criterion enabled the analysis to focus on low-elevation areas potentially associated with flood dynamics and to exclude higher-elevation areas, improving the spatial consistency of subsequent analyses.

2.4. SAR Data and Processing

Flood detection was based on analyzing Sentinel-1 Ground Range Detected (GRD) images, acquired in Interferometric Wide Swath (IW) mode with dual VH and VV polarization, available in the COPERNICUS/S1_GRD collection [37]. Images were selected from ascending relative orbit 18. Among the eight retained events, acquisitions were from Sentinel-1B for E01, E04, E06, and E08, and Sentinel-1A for E10, E11, E12, and E13.

The images were used in their calibrated and terrain-corrected form, according to the standard preprocessing pipeline for the COPERNICUS/S1_GRD collection in GEE [38]—which also includes orbit correction and removal of border and thermal noise—without any additional radiometric or geometric processing prior to change analysis. A focal mean filter with a circular kernel of 50 m radius was subsequently applied to reduce speckle noise [20].

The Copernicus GLO-30 DEM, used for topographic constraining of detection, and the MapBiomas Peru LULC product were incorporated as auxiliary variables. The analysis period spanned from 2019 to 2025, and the acquisition parameters are summarized in Table 1.

Table 1. Acquisition and preprocessing parameters for Sentinel-1 imagery and ancillary datasets.

Parameter	Value	Source/Collection ID
Sensor	Sentinel-1B (E01–E08); Sentinel-1A (E10–E13)	ESA Copernicus
Product	Ground Range Detected (GRD)	COPERNICUS/S1_GRD
Acquisition mode	IW	—
Polarization	VV and VH	—
Relative orbit	18, ascending	—
Pixel spacing	10 m	—
Backscatter coefficient	σ^0 (dB)	—
Period	2019–2025	—
DEM	Copernicus DEM GLO-30	COPERNICUS/DEM/GLO30 [36]
LULC	MapBiomas Peru, Collection 3	projects/mapbiomas-public/assets/peru/collection3/mapbiomas_peru_collection3_integration_v1

The images were analyzed using the backscatter coefficient σ^0, since the Sentinel-1 GRD dataset available on GEE provides calibrated and geometrically corrected values in this radiometric convention [39]. Although γ^0 can reduce the dependence of backscatter on local incidence geometry, the analysis was restricted to surfaces with slopes ≤5°, reducing the influence of topographic effects within the study area. Consequently, σ^0 was used as the radiometric variable to distinguish between flooded and non-flooded surfaces.

2.5. Catalog of Events and Time Frames

A catalog of flood events for the 2019–2025 period was compiled using official records from the National Institute of Civil Defense (INDECI), available in the National Information System for Response and Rehabilitation (SINPAD v2.0) [40] and the Peruvian flood-event inventory published by SENAMHI [41]. Event-specific PRE and POST query windows were defined relative to the cataloged event date to generate the baseline and event-observation composites, respectively (Table 2).

Table 2. Catalog of flood events and temporal windows used to generate the PRE and POST Sentinel-1 composites.

Event	Cataloged Event Date	PRE Start	PRE End	POST Start	POST End	Last PRE Acquisition	Interval to Event Date (Days)
E01	25 February 2019	1 January 2019	20 February 2019	22 February 2019	5 March 2019	31 January 2019	25
E02	20 March 2019	15 January 2019	15 March 2019	18 March 2019	30 March 2019	—	—
E03	25 April 2019	15 January 2019	15 March 2019	23 April 2019	5 May 2019	—	—
E04	18 October 2019	15 August 2019	14 October 2019	16 October 2019	28 October 2019	10 October 2019	8
E05	18 December 2019	15 October 2019	14 December 2019	16 December 2019	28 December 2019	—	—
E06	4 June 2020	1 April 2020	30 May 2020	1 June 2020	15 June 2020	25 May 2020	10

Table 2. *Cont*.

Event	Cataloged Event Date	PRE Start	PRE End	POST Start	POST End	Last PRE Acquisition	Interval to Event Date (Days)
E07	12 March 2021	10 January 2021	8 March 2021	10 March 2021	22 March 2021	—	—
E08	28 November 2021	25 September 2021	12 November 2021	28 November 2021	8 December 2021	4 November 2021	24
E09	3 March 2022	15 December 2021	28 February 2022	1 March 2022	15 March 2022	—	—
E10	15 March 2023	10 January 2023	10 March 2023	13 March 2023	25 March 2023	5 March 2023	10
E11	27 December 2023	25 October 2023	22 December 2023	25 December 2023	6 January 2024	18 December 2023	9
E12	15 February 2025	15 December 2024	10 February 2025	12 February 2025	25 February 2025	29 January 2025	17
E13	2 March 2025	1 January 2025	11 February 2025	28 February 2025	10 March 2025	10 February 2025	20

Note: PRE and POST start and end dates delimit the temporal queries and do not necessarily correspond to acquisition dates. The last PRE acquisition and its interval to the cataloged event date are reported for the eight retained events; dashes indicate events excluded from the final analysis.

The PRE composite was the temporal median of at least three available Sentinel-1 scenes within the event-specific query window in Table 2. The POST composite was the temporal median of the available scenes in the corresponding window, with a minimum of one scene. Query-window boundaries do not necessarily coincide with acquisition dates. Table 2 also reports the last PRE acquisition and its interval to the cataloged event date for the eight retained events. Scene counts can include adjacent scenes acquired on the same date; for E08, the two POST scenes were acquired on 28 November 2021. The E08 POST window starts on the cataloged event date, so the composite includes only acquisitions from that date onward.

2.6. Flood Detection Based on Backscatter Changes

Flood detection was based on the analysis of backscatter changes between the PRE and POST composites, with the backscatter difference defined as POST–PRE [42–44]. Three change variables were calculated: VH, VV, and the combination of dual polarization $(VH+VV)^2$ [16]. The latter was calculated independently for the PRE and POST sets, according to: (1) conversion of the VH and VV values from decibels (dB) to a linear power scale; (2) calculation of the combination $(VH_{lin} + VV_{lin})^2$; and (3) reconversion of the result to decibels. The POST−PRE backscatter difference for this combined variable was subsequently calculated on a logarithmic scale, following the same criteria applied to VH and VV. This procedure avoided combining polarizations directly on values expressed on a logarithmic scale [20].

2.7. Otsu's Automatic Thresholding Technique

Otsu thresholding was applied separately to each difference image to partition its histogram by maximizing between-class variance [13,45]. The histogram calculation was restricted to surfaces with slopes ≤5°, derived from the Copernicus GLO-30 DEM [36]. This restriction allowed the analysis to be limited to the areas topographically compatible with the occurrence of flooding and reduced the influence of steep slopes on the distribution of backscatter values [17,18].

2.8. Post-Processing Filters

The initial binary map was refined using a sequence of spatial filters applied after classification. First, a slope mask (≤5°) and a permanent water mask were applied; the latter was generated by digitizing the active channel annually using Sentinel-2 imagery acquired during the dry season to exclude water bodies not associated with flooding events [45]. A 1000 m buffer around the digitized main channel and secondary tributaries was then applied to restrict detections to the river corridor. Finally, a minimum mapping unit (MMU) of eight connected pixels, equivalent to 0.08 ha, was established to eliminate isolated clusters of smaller area [46]. The resulting maps were exported, with pixels classified as non-flooded retained as "NoData," in accordance with the procedure defined for the subsequent multitemporal recurrence analysis. The complete detection workflow for a representative event (E13, March 2025) is shown in Figure 3.

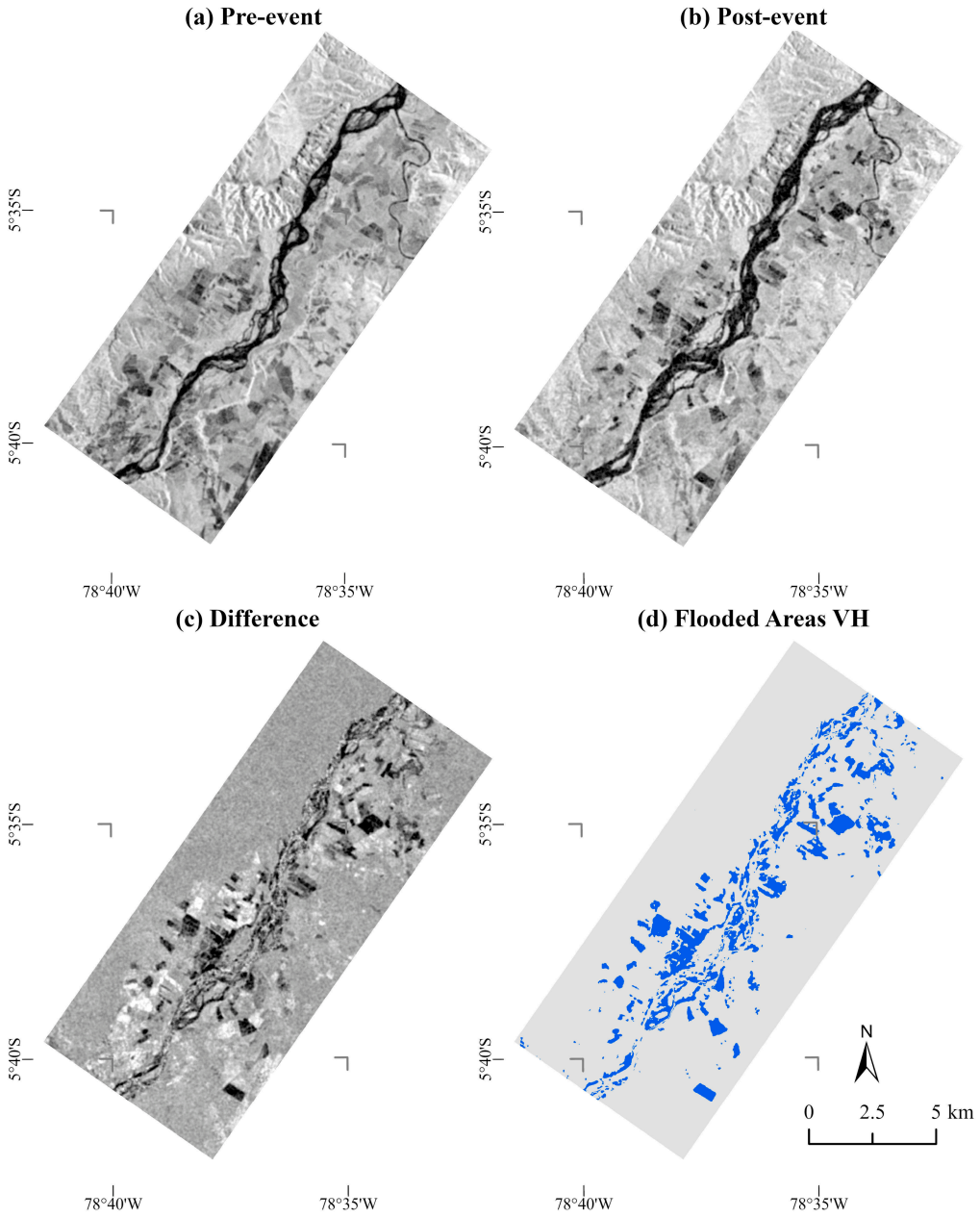


Figure 3. SAR flood detection for event E13. (**a**) Pre-event composite (VH); (**b**) post-event image (VH); (**c**) VH difference image; (**d**) flood map after Otsu thresholding and topographic filtering.

2.9. Event Quality Control

Before inclusion in the multitemporal analysis, the 13 cataloged events were evaluated using three quality-control criteria. First, VH Otsu thresholds near −0.70 dB, compared with values near −2.80 dB in the retained events, were considered anomalous when assessed together with difference histograms and binary maps. This was an empirical radiometric plausibility check, not a statistical test of bimodality. Second, events were excluded when their PRE reference window overlapped with a previously cataloged flood. Third, spatial plausibility and temporal representativeness were examined, excluding detections that covered nearly all flat terrain in the valley or POST observations representing an advanced recession phase.

The first and third criteria were assessed through expert inspection of histograms and detection maps; the second used the dates of previously cataloged events. Eight events met all three criteria: E01, E04, E06, E08, E10, E11, E12, and E13. Exclusion reasons are listed in Table 3. Because the first criterion used VH threshold behavior, the dispersion of VH in the retained subset is conditioned by event selection and does not independently establish superiority over VV or the combined variable.

Table 3. Numbers of PRE and POST Sentinel-1 scenes, Otsu thresholds (dB) for each variable, and inclusion status of the 13 cataloged events. Multiple scenes may correspond to the same acquisition date.

Event	PRE Scenes	POST Scenes	VH	VV	(VH+VV)^2	Status
E01	6	2	−2.82	−0.70	−2.79	Included
E02	8	2	−2.86	−2.82	−4.90	Excluded [1]
E03	8	2	−0.70	−0.68	−0.82	Excluded [2]
E04	10	2	−2.77	−0.70	−2.75	Included
E05	10	2	−0.72	−0.71	−2.86	Excluded [1]
E06	10	2	−2.78	−2.73	−6.90	Included
E07	8	2	−0.68	−0.72	−0.84	Excluded [2]
E08	8	2	−2.80	−2.72	−2.80	Included
E09	3	1	−0.74	−0.73	−0.87	Excluded [2]
E10	5	1	−2.85	−2.75	−2.81	Included
E11	5	1	−2.88	−2.86	−2.87	Included
E12	4	1	−2.87	−0.69	−2.84	Included
E13	4	1	−2.89	−0.69	−2.86	Included

[1] Excluded because the PRE window overlapped with a previously recorded flood. [2] Excluded because of anomalous VH threshold behavior, according to the radiometric plausibility criterion described in Section 2.9.

2.10. Observed Flood Recurrence Map

Observed recurrence was calculated by counting, for each pixel, the retained event maps in which it was classified as flooded. Counts were grouped into five classes: very low (one event), low (two), moderate (three), high (four), and very high (five to seven, the observed maximum). These classes are relative to the eight cataloged events and do not represent annual probabilities or return periods. The raster was vectorized and features were dissolved by class into single-part geometries. The principal area estimates were calculated from these polygons in ArcGIS Pro 3.5.4 using WGS 84/UTM zone 18S (EPSG:32718). Raster counts used in sensitivity analyses are reported separately from these polygon-based estimates.

2.11. Accuracy Assessment and Spatial Context

Quantitative validation was performed for event E13, as it was the only event in the series for which a post-event Sentinel-2 image was available with adequate visibility

conditions to generate reference data through visual interpretation. For the other events, extensive cloud cover in the optical acquisitions near the flood dates limited the ability to obtain comparable reference data. Therefore, quantitative evaluation using a confusion matrix was applied to E13, while the other events underwent the quality control procedures described in Section 2.9.

The eligible detection domain for E13 was the intersection of the study area, the 1000 m hydrographic buffer, and the slope mask ($\leq 5°$), excluding the permanent channel. It covered 22,696.25 ha within the 74,424.00 ha study area. Reference sampling covered only the cloud-free sectors in which reference polygons could be delineated; the resulting metrics are not estimates for the entire eligible domain or valley.

Flooded and non-flooded reference polygons were digitized by visual interpretation of post-event Sentinel-2 imagery within the eligible domain, excluding cloud-covered areas. A random sample of 680 points per reference class yielded 1360 points. The classifications from VH, VV, and $(VH+VV)^2$ were extracted at the same points. Documentary flood records and a field campaign in May 2026 provided complementary context. Three areas with high observed recurrence were surveyed using field photographs and a DJI Matrice 4E with RTK at a flight altitude of 300 m. Photogrammetric processing in Agisoft Metashape Professional V2.2.1 (Agisoft; Agisoft LLC, St. Petersburg, Russia) produced orthomosaics at approximately 8 cm per pixel and DEMs at approximately 16 cm per pixel. These products characterized local terrain and river–floodplain relationships; the time lag precluded their use as reference data for the historical event extents.

Confusion matrices for VH, VV, and $(VH+VV)^2$ were constructed using the same reference sample. Overall accuracy (OA), flooded-class user's accuracy (UA), and flooded-class producer's accuracy (PA) were calculated directly from the sample counts, without area weighting, using Equations (1)–(3):

$$\mathrm{OA} = \frac{TP + TN}{N} \times 100 \tag{1}$$

$$\mathrm{UA} = \frac{TP}{TP + FP} \times 100 \tag{2}$$

$$\mathrm{PA} = \frac{TP}{TP + FN} \times 100 \tag{3}$$

Here, TP denotes flooded reference points correctly classified as flooded; TN denotes non-flooded points correctly classified as non-flooded; FP denotes non-flooded points classified as flooded; and FN denotes flooded points classified as non-flooded. N is the total number of reference points. OA, UA, and PA are expressed as percentages.

The flooded-class F1 score was calculated from the confusion-matrix counts using Equation (4) and reported on a scale from 0 to 1:

$$\mathrm{F1} = \frac{2TP}{2TP + FP + FN} \tag{4}$$

Specificity was calculated as TN/(TN + FP), and Cohen's Kappa was retained as a supplementary measure based on observed agreement and agreement expected from the sample marginal proportions. The 95% confidence intervals for PA and specificity were calculated using the Wilson score method [47], treating observations within each reference class as independent Bernoulli trials. These intervals quantify binomial sampling uncertainty and do not account for spatial dependence or uncertainty in the reference labels. OA, UA, F1, and Kappa describe the balanced sample and were not interpreted as area-weighted estimates of accuracy across the study area. Area-weighted estimates were not reported because the sample was stratified by reference class within cloud-free sectors digitized on Sentinel-2, rather than by map class over the study area. In addition, the population proportions required for area weighting were not available.

A complementary spatial analysis compared detections among seven slope classes within the eligible domain, excluding the permanent channel. For each class, its share of detected area was divided by its share of available area. Ratios above one indicate greater representation among detections than expected from available area, whereas ratios below one indicate lower representation. The calculation was performed for the area detected at least once and separately for each retained event. It characterizes the distribution of detections within the imposed spatial constraints and is not an independent accuracy assessment.

2.12. Exposure Analysis by Land Use and Land Cover (LULC)

The observed recurrence map was overlaid with MapBiomas Peru Collection 3 for 2024 to quantify the area of each land-cover class within the recurrence classes. The 2024 layer was the latest year in the collection used for this study. The overlay characterizes exposure of the land covers represented in 2024 to detections from 2019 to 2025; it does not reconstruct land cover at each historical event or land-cover change over the study period.

A complementary analysis summed detections by land-cover class across individual events, using the classification for each event year. E12 and E13 used the 2024 layer because the collection used did not include 2025. A surface detected in several events contributes to the sum several times; this cumulative quantity is expressed in hectare-events and differs from the unique area detected at least once. The flood maps were processed at 10 m, whereas MapBiomas has a 30 m grid. Exposure estimates from the LULC cross-tabulation therefore use a different spatial representation from the polygon-based flood areas, particularly along boundaries.

2.13. Sensitivity Analysis

The sensitivity of the area detected as flooded to hydrographic buffer distance and maximum slope was evaluated for the eight retained events by varying one parameter at a time. Buffer distance ranged from 500 to 1500 m in 250 m increments, with the maximum slope fixed at 5°. Maximum slope ranged from 3° to 7° in 1° increments, with the buffer fixed at 1000 m. All other parameters were held constant. The Otsu threshold was recalculated for each slope configuration because changing this constraint modifies the histogram domain. For each configuration, detected areas were summed across the eight events, counting an area again whenever it was detected in another event. Changes in this cumulative area were expressed as percentages relative to the reference configuration of a 1000 m buffer and a 5° maximum slope.

Sensitivity to PRE timing was examined by setting the end of the PRE query window to 15 days before the cataloged event date, while keeping its start date and the POST window unchanged. The comparison focused on whether this adjustment changed the scenes included in the PRE composite and the resulting VH and VV Otsu thresholds relative to the original configuration.

An additional sensitivity analysis examined the influence of events outside the main wet season by retaining only the five events within December–April and excluding E04, E06, and E08. This subset was compared with the eight-event dataset in terms of land-cover composition, raster-based area detected at least once, and the spatial concentration of pixels with at least four detections. The same absolute threshold of four detections was used in both datasets, and spatial concentration was assessed as the proportion of this area located within 15 km of the Utcubamba–Marañón confluence (Supplementary Table S1).

3. Results

3.1. Otsu Threshold Dispersion and Polarization Selection

Across the eight retained events, the Otsu thresholds for the VH difference had a mean of −2.83 dB and a standard deviation of 0.05 dB. VV had a mean of −1.73 dB and a standard deviation of 1.11 dB, whereas the combined index $(VH+VV)^2$ had a mean of −3.33 dB and a standard deviation of 1.44 dB (Table 3). Within this subset, VH exhibited the lowest variability among the three variables evaluated.

When all 13 cataloged events were considered, the means and standard deviations were -2.18 ± 1.02 dB for VH, -1.50 ± 1.05 dB for VV, and -2.84 ± 1.65 dB for $(VH+VV)^2$.

When the end of the PRE window was set to 15 days before the cataloged event date, E01 and E12 retained the acquisitions used in the original configuration. For E04, E10, and E11, this modification resulted in changes of up to 0.04 dB in the VH and VV thresholds.

3.2. Event-Specific Detection Patterns

The eight retained maps differed in detected extent during 2019–2025 (Figure 4). Individual areas ranged from 1855.76 ha for E11 to 2674.22 ha for E08. Their sum was 17,793.06 hectare-events, with a mean of 2224.13 ha per event. Table 4 reports the polygon-based areas and each event's contribution to the cumulative sum.

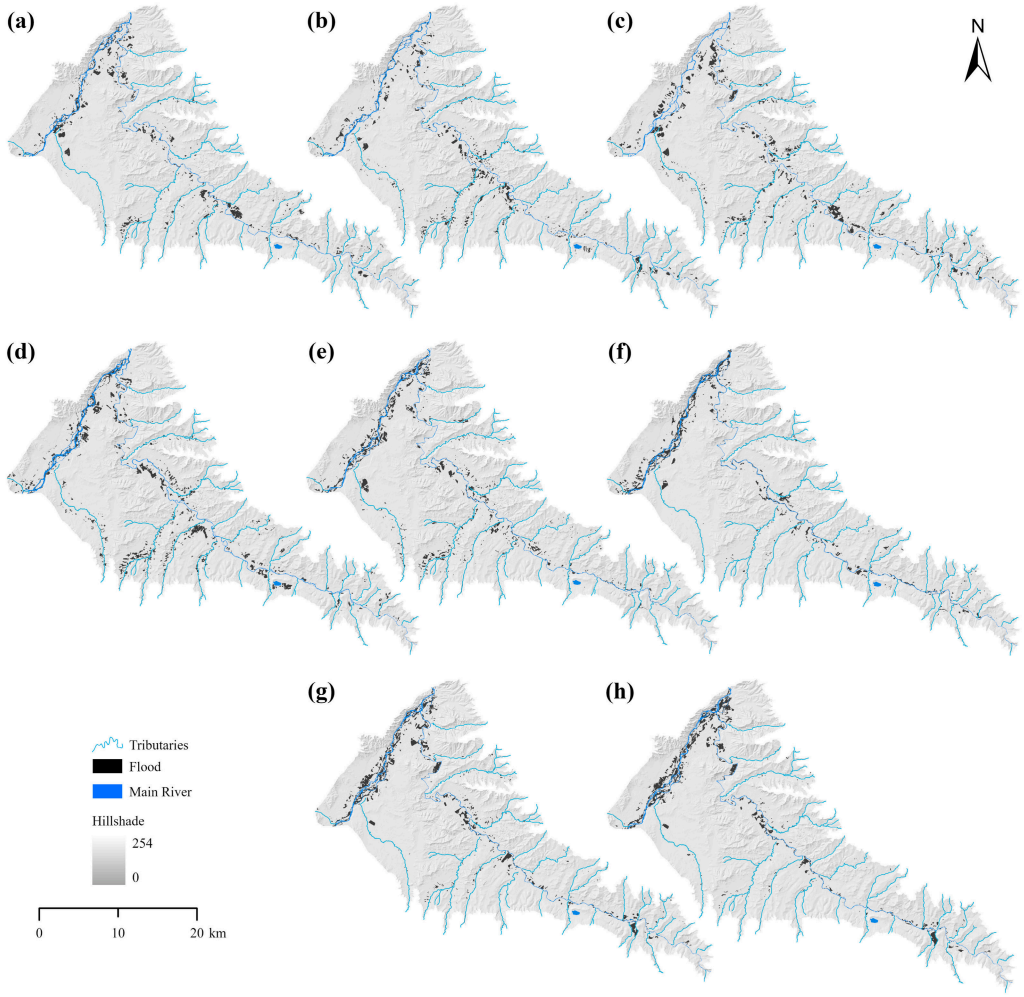


Figure 4. Flood maps for the eight retained events: (**a**) E01 (25 February 2019), (**b**) E04 (18 October 2019), (**c**) E06 (4 June 2020), (**d**) E08 (28 November 2021), (**e**) E10 (15 March 2023), (**f**) E11 (27 December 2023), (**g**) E12 (15 February 2025), and (**h**) E13 (2 March 2025).

Table 4. Area detected as flooded and relative contribution of the eight retained flood events analyzed during 2019–2025.

Event	Cataloged Event Date	Area Detected as Flooded (ha)	Contribution (%)
E01	25 February 2019	1915.76	10.77
E04	18 October 2019	1958.30	11.01
E06	4 June 2020	2540.39	14.28
E08	28 November 2021	2674.22	15.03
E10	15 March 2023	2238.63	12.58
E11	27 December 2023	1855.76	10.43
E12	15 February 2025	2401.15	13.49
E13	2 March 2025	2208.85	12.41
Total	—	17,793.06	100.00
Mean	—	2224.13	—

Detections were concentrated in the northern sector of the valley, where the alluvial plain is wider. Smaller extents were mapped along the more confined southern river corridor. Although event-specific extents differed, repeated detections occurred in several of the same sectors.

3.3. Observed Flood Recurrence

The integration of the eight retained event maps identified 9842.02 ha detected as flooded at least once within the study area during 2019–2025 (Figure 5). Very low recurrence, corresponding to detection in one event, covered 4860.89 ha (49.39%), while low recurrence, corresponding to two detections, covered 2887.00 ha (29.33%). Together, these classes accounted for 78.72% of the total detected area. Moderate recurrence, corresponding to three detections, covered 1475.26 ha (14.99%). High recurrence, corresponding to four detections, represented 483.28 ha (4.91%), and very high recurrence, corresponding to five to seven detections, covered 135.59 ha (1.38%).

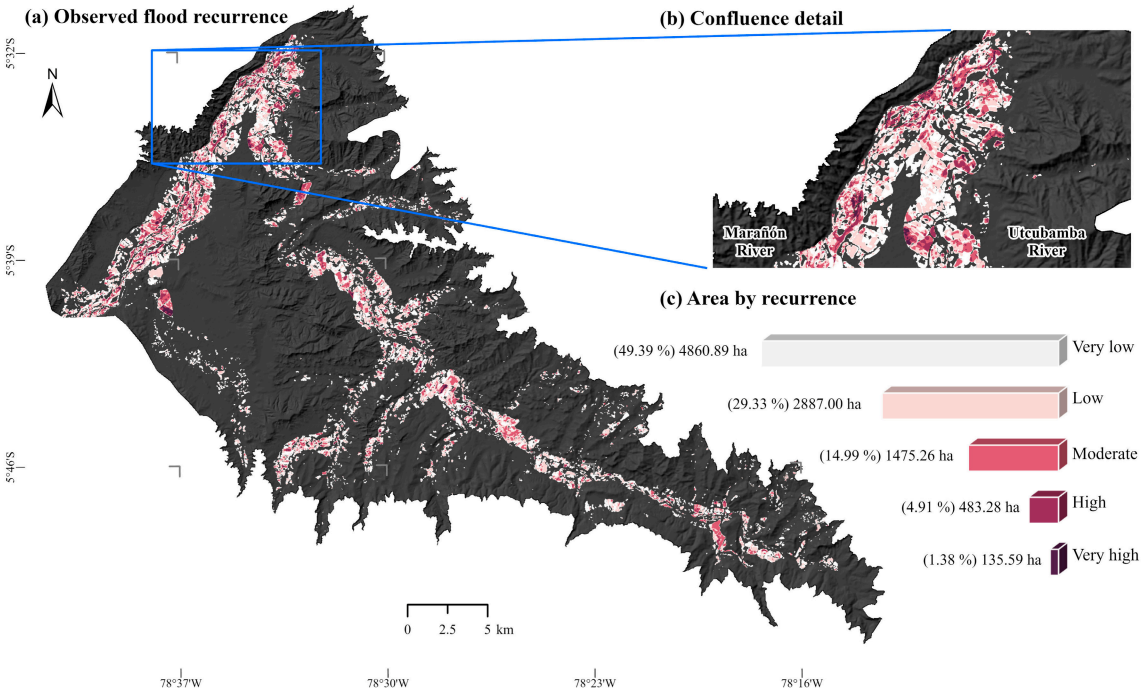


Figure 5. Observed flood recurrence map of the Utcubamba River Valley (2019–2025).

High and very high recurrence jointly covered 618.87 ha (6.29%) and were concentrated near the Utcubamba–Marañón confluence and along meanders in the northern valley. These classes represent repeated detections among the eight retained cataloged events.

3.4. Accuracy Assessment of E13 and Spatial Context

E13 was evaluated using 1360 reference points, comprising 680 flooded and 680 non-flooded points derived from visual interpretation of Sentinel-2 imagery. For VH, the confusion matrix contained 526 true positives, 632 true negatives, 48 false positives, and 154 false negatives. Sample-based overall accuracy was 85.15%, user's accuracy for the flooded class was 91.64%, and producer's accuracy was 77.35% (95% CI: 74.06–80.34%). Specificity reached 92.94% (95% CI: 90.77–94.63%), the F1 score was 0.839, and the Kappa coefficient was 0.703.

When evaluated against the same reference points, VV achieved a sample-based overall accuracy of 80.66%, a user's accuracy of 84.92%, a producer's accuracy of 74.56%, and an F1 score of 0.794. The corresponding values for the $(VH+VV)^2$ index were 80.37%, 90.25%, 68.09%, and 0.776, respectively. VH had the highest point estimates for the reported accuracy metrics; differences were evaluated descriptively (Table 5).

Table 5. Accuracy metrics for VH, VV, and $(VH+VV)^2$ for event E13, evaluated using the same balanced sample of 1360 reference points.

Metric	VH	VV	$(VH+VV)^2$
True positives	526	507	463
True negatives	632	590	630
False positives	48	90	50
False negatives	154	173	217
Sample-based overall accuracy (%)	85.15	80.66	80.37
User's accuracy, flooded class (%)	91.64	84.92	90.25
Producer's accuracy, flooded class (%)	77.35	74.56	68.09
Producer's accuracy 95% CI (%)	74.06–80.34	71.15–77.69	64.49–71.48
Specificity (%)	92.94	86.76	92.65
Specificity 95% CI (%)	90.77–94.63	84.01–89.11	90.44–94.38
Sample-based F1 score	0.839	0.794	0.776
Sample-based Cohen's Kappa	0.703	0.613	0.607

Note: All metrics were calculated from the sample confusion matrices without area weighting. Each reference class comprised 680 points. The 95% confidence intervals (CIs) were estimated using the Wilson method.

High-resolution UAV-derived DEMs, with a pixel size of approximately 16 cm, showed that mapped high-recurrence sectors occupied low-lying parts of the alluvial plain in the three surveyed areas (Figure 6). These products provided detailed geomorphological context at a finer scale than the 30 m DEM.

The UAV-derived slope maps showed a predominance of terrain with slopes below 5° in the three surveyed areas (Figure 7). These gently sloping surfaces coincided spatially with sectors of high observed recurrence and characterized their local topographic setting.

The concentration ratio of flood detections decreased progressively with slope, from 1.63 in the 0–0.5° class to 0.49 in the 4–5° class (Figure 8). Classes with slopes below 1.5° had ratios greater than 1, whereas the remaining classes had ratios below 1. A decreasing gradient was also observed in each of the eight events.

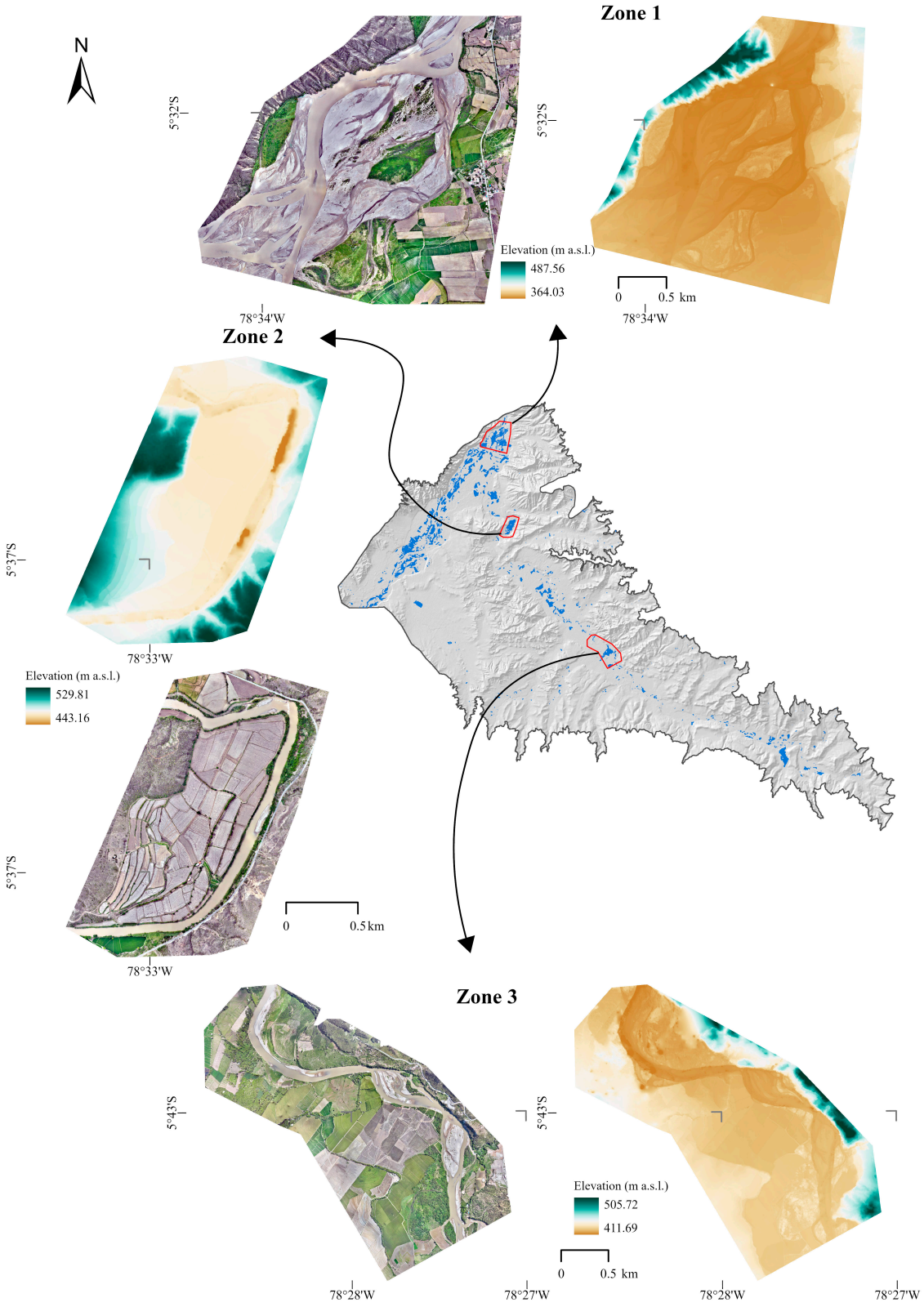


Figure 6. Geomorphological characterization of the three surveyed areas using orthomosaics and high-resolution DEMs obtained with an RTK drone.

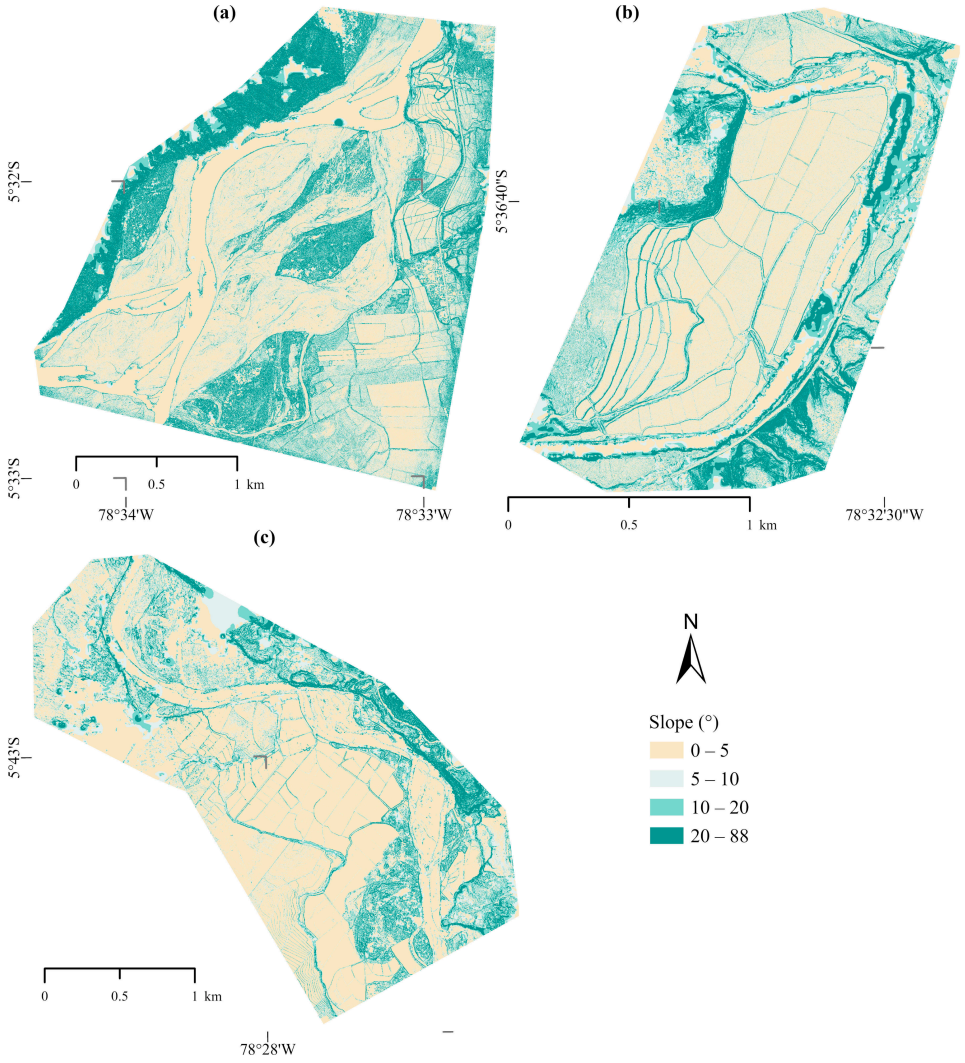


Figure 7. Spatial distribution of slopes in the three surveyed areas derived from high-resolution digital elevation models: (**a**) Zone 1, (**b**) Zone 2, and (**c**) Zone 3.

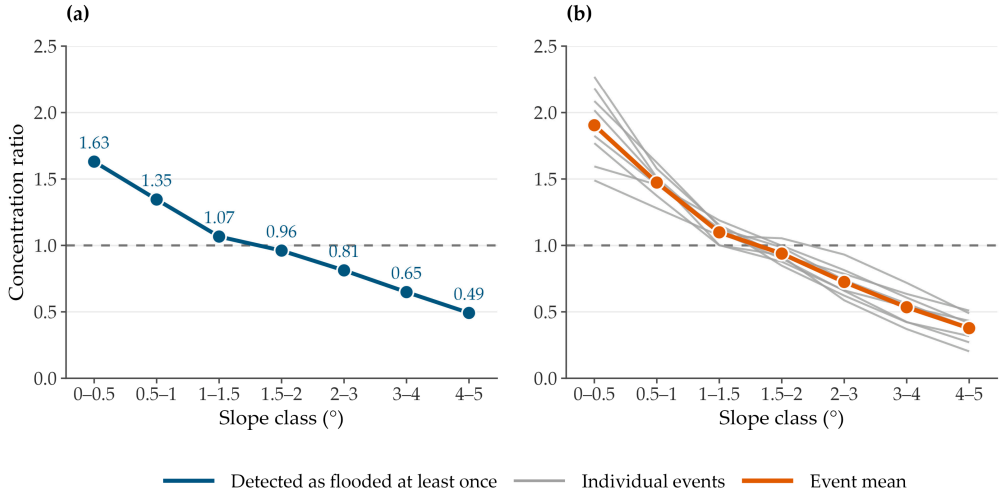


Figure 8. Concentration of the area detected as flooded across slope classes within the eligible domain: (**a**) area detected as flooded at least once across the eight events; (**b**) individual events and their arithmetic mean. The concentration ratio was calculated by dividing each class's share of the flooded area by its share of the available area. The dashed horizontal line at 1 indicates a distribution proportional to the available area.

3.5. Field Observations of River–Floodplain Conditions

The field campaign documented local river–floodplain conditions in the three surveyed areas (Figure 9). In Zone 1, at the Utcubamba–Marañón confluence, a marked lateral expansion of the flow was observed, facilitated by the width of the floodplain and the meandering morphology of the Marañón River. This pattern is consistent with a possible backwater effect at the confluence, which aligns with the higher recurrence observed in this sector compared to the rest of the valley.

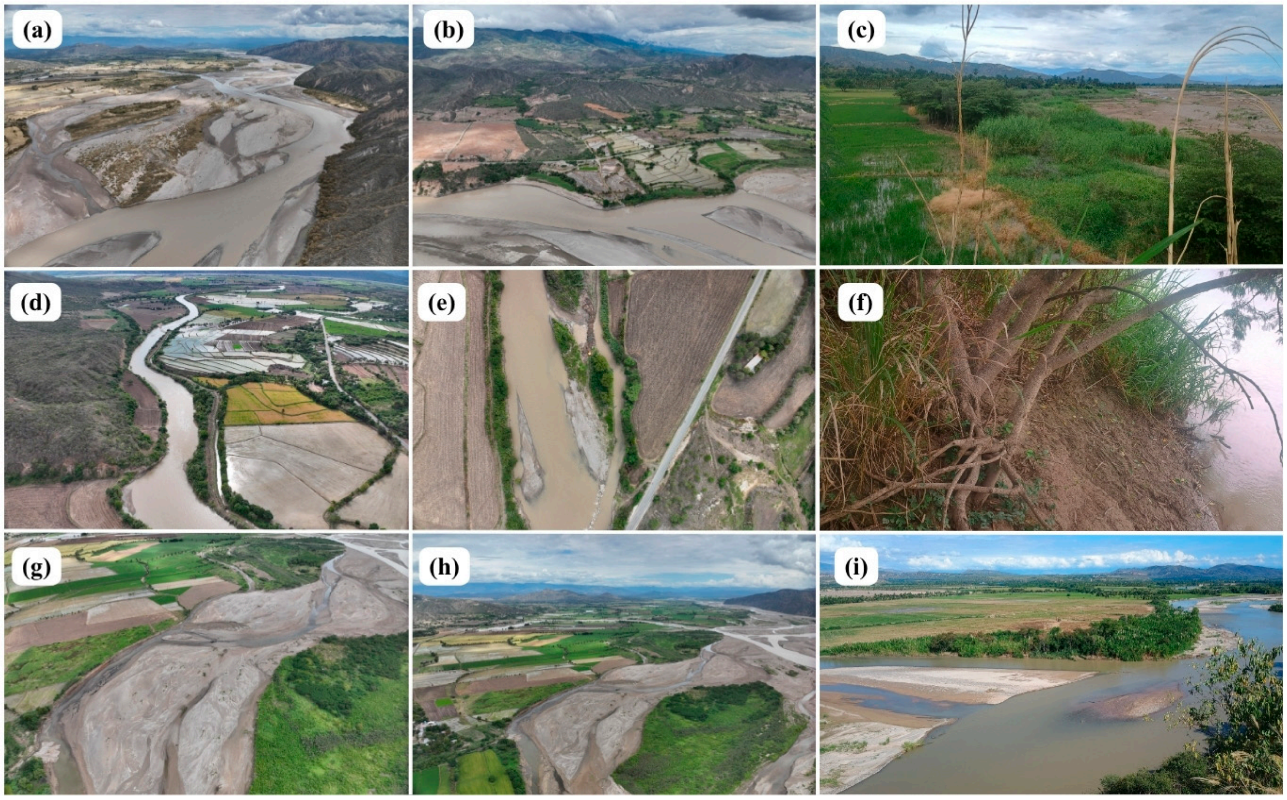


Figure 9. Field evidence of river dynamics and associated impacts. (**a**–**c**) Zone 1, lateral overflow and pooling at the confluence; (**d**–**f**) Zone 2, connection between the channel and plots and bank erosion; (**g**–**i**) Zone 3, low-lying plain and lateral channel migration.

In Zone 2, a direct connection between the river channel and agricultural plots was documented, together with exposed roots of riparian vegetation associated with bank erosion and water intake infrastructure at channel level. Uncultivated plots with remaining agricultural infrastructure were also observed. In Zone 3, field observations documented a broad, gently sloping plain and evidence of lateral channel migration adjacent to rice-growing areas.

The surveyed areas combined low-lying floodplain terrain, agricultural land use, and local connections between channels and cultivated plots. These observations provide context for interpreting the spatial distribution of detections, but do not establish the causes of individual historical detections or quantify agricultural damage.

3.6. Exposure of Land Cover to Floods

Overlaying the observed flood recurrence map with the 2024 MapBiomas land-cover data showed that mapped exposure was concentrated in agricultural systems (Table 6). Rice accounted for 5341.23 ha (54.25%) of the total overlay area, followed by agricultural mosaic with 1915.74 ha (19.46%). Together, these agricultural classes represented 73.70% of

the total. Beach and river, lake or ocean classes jointly accounted for 1581.39 ha (16.06%), whereas urban infrastructure represented 54.09 ha (0.55%).

Table 6. Distribution of the area detected as flooded (ha) by MapBiomas land cover class and recurrence level, with total area and percentage by land cover.

Land-Cover Class	Very Low	Low	Moderate	High	Very High	Total Area (ha)	% of Total
Rice	2532.24	1717.11	831.96	218.97	40.95	5341.23	54.25
Agricultural mosaic	1095.93	517.5	234.72	51.93	15.66	1915.74	19.46
Beach	208.62	231.21	222.03	130.41	49.86	842.13	8.55
Dry forest	404.28	97.92	27.99	5.13	4.05	539.37	5.48
Other natural areas without vegetation	251.55	82.44	27.27	6.84	3.24	371.34	3.77
River, lake or ocean	294.48	221.31	132.21	68.67	22.59	739.26	7.51
Other non-forested land	29.61	8.01	0.45	0.00	0.00	38.07	0.39
Urban infrastructure	45.27	6.12	2.34	0.36	0.00	54.09	0.55
Other land cover	4.23	0.72	0.09	0.00	0.00	5.04	0.05
Total	4866.21	2882.34	1479.06	482.31	136.35	9846.27	100

Note: Percentages were calculated relative to the total land-cover overlay area of 9846.27 ha.

The very low and low recurrence classes jointly accounted for most of the detected area within each land-cover class. Beach areas represented 8.55% of the total overlay area and included 180.27 ha in the high and very high recurrence classes. Rice occupied the largest absolute area in the very low, low, moderate, and high recurrence classes. In the very high recurrence class, beach areas predominated with 49.86 ha, followed by rice with 40.95 ha (Table 6).

3.7. Cumulative Flood Exposure by Land Cover

The integration of the eight retained events allowed cumulative exposure to be quantified for each land-cover class by summing the flooded areas across individual events (Figure 10). Rice had the highest cumulative exposure, with 9988 ha-events (56.06% of the total), followed by agricultural mosaic with 2913 ha-events (16.35%) and beach areas with 2407 ha-events (13.51%). Together, these three classes accounted for approximately 85.9% of the cumulative flooded area. River/lake areas accounted for 1274 ha-events (7.15%), followed by dry forest with 697 ha-events (3.91%) and other natural areas with 407 ha-events (2.28%). Other non-forested land, urban infrastructure, and other land-cover classes jointly represented 0.73% of cumulative exposure.

The cumulative flooded area obtained from the LULC cross-tabulation was 17,814.69 ha-events, differing by 21.63 ha-events (0.12%) from the 17,793.06 ha-events calculated directly from the eight flood maps (Section 3.2). This small difference resulted from the spatial overlay of the flood maps processed at 10 m with the MapBiomas LULC dataset at 30 m, which altered the representation of flooded boundaries on the analysis grid.

Agricultural classes accounted for 84% of cumulative detected area across the three events outside the main wet season (E04, E06, and E08), compared with 64% across the five wet-season events, whereas beach and river/lake classes accounted for 7% and 30% in these two groups, respectively (Supplementary Table S2). About 54% of the area detected in the three out-of-season events was not detected in any wet-season event (Supplementary Table S3). In the supplementary raster analysis, 69% of the area with at least four detections in the five-event subset lay within 15 km of the Utcubamba–Marañón

confluence, compared with 61% in the eight-event analysis (Supplementary Table S1). The same absolute threshold of four detections was used in both scenarios. These results describe the composition and spatial distribution of detections; they do not estimate irrigation-related false-positive rates.

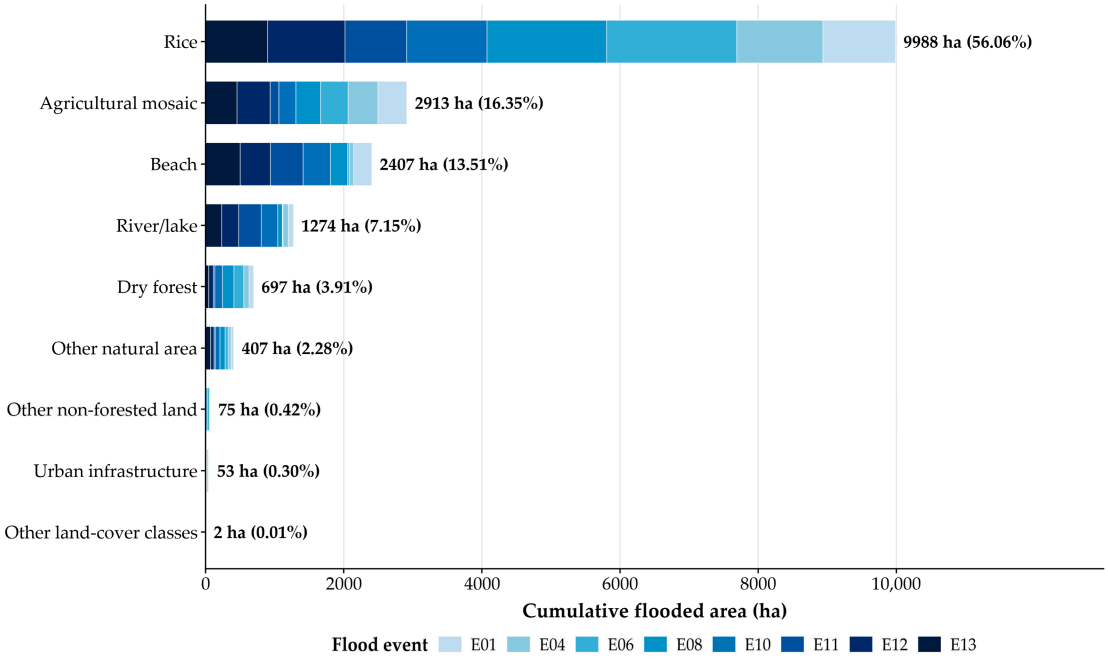


Figure 10. Cumulative detected area by land-cover class and contribution of the eight retained events, expressed in hectare-events.

3.8. Sensitivity of Detected Flooded Area to Processing Parameters

With the maximum slope fixed at 5°, the summed detected area varied from −30.7% at a 500 m hydrographic buffer to +15.4% at a 1500 m buffer, relative to the reference configuration of 1000 m. The corresponding changes at 750 and 1250 m were −12.8% and +9.0%, respectively (Table 7).

Table 7. Change in the summed detected area with the hydrographic buffer distance, relative to the reference configuration (1000 m), with the maximum slope fixed at 5°.

Buffer Distance (m)	Change Relative to Reference (%)
500	−30.7
750	−12.8
1000	0.0
1250	+9.0
1500	+15.4

With the hydrographic buffer fixed at 1000 m, the summed detected area varied from −14.7% at a maximum slope of 3° to +7.2% at 7°, relative to the reference configuration of 5° (Table 8). VH Otsu thresholds ranged from −2.90 to −2.75 dB across the 40 event–slope combinations evaluated.

Table 8. Change in the summed detected area with the maximum slope, relative to the reference configuration (5°), with the hydrographic buffer distance fixed at 1000 m.

Maximum Slope (°)	Change Relative to Reference (%)
3	−14.7
4	−5.9
5	0.0
6	+4.1
7	+7.2

4. Discussion

The comparison of the three SAR variables supports the selection of VH under the conditions evaluated in the Utcubamba Valley. Among the eight retained events, VH thresholds showed lower dispersion (−2.83 ± 0.05 dB) than VV (−1.73 ± 1.11 dB) and $(VH+VV)^2$ (−3.33 ± 1.44 dB). Previous research has identified the potential of VH for mapping flooded crops [19], while applications in the Caprivi floodplain and Mekong Delta illustrate the use of Sentinel-1 time series for monitoring inundation across different landscape conditions [48,49]. Polarization combinations have also been investigated as alternatives for flood mapping [16,20]. A multi-event evaluation also identified differences associated with polarization, particularly over vegetation and under windy conditions, indicating that performance must be interpreted in relation to the observed surface conditions [50]. Here, the low dispersion of VH thresholds characterizes the retained dataset but does not independently establish greater temporal stability because event selection partly depended on VH threshold behavior. This result must therefore be considered alongside the full 13-event statistics and the assessment against reference data.

The E13 assessment provided complementary support for using VH. Against the same reference sample, VH produced fewer commission and omission errors than VV; compared with $(VH+VV)^2$, its main advantage was a lower omission rate for flooded reference points. Thus, combining the polarizations did not improve the reported accuracy metrics for this event. Nevertheless, VH omitted 22.65% of the flooded reference points, showing that the selected variable still failed to detect a substantial proportion of the reference inundation. The differences among variables were evaluated descriptively, without tests of statistical significance. OA, UA, and F1 characterize the balanced sample and were not interpreted as area-weighted estimates of accuracy across the study area, consistent with the need to align accuracy estimators with the sampling design [51]. Moreover, suitable Sentinel-2 imagery restricted the quantitative assessment to cloud-free sectors of E13. The other seven events underwent the quality controls described in Section 2.9, but these controls do not provide equivalent estimates of classification accuracy. The spatial and temporal coverage of the reference data therefore defines the scope of the assessment [51,52].

The spatial analysis extends this event-level comparison by identifying where detections repeatedly occurred. Although 78.72% of the area detected at least once appeared in only one or two events, high and very high observed recurrence was concentrated near the Utcubamba–Marañón confluence and northern valley meanders. Field observations and UAV-derived terrain models provide geomorphological context for these detections in low-lying sectors of the alluvial plain. Normalizing detections by the available area in each slope subclass further revealed differences in their concentration within the eligible domain. These findings help interpret the spatial pattern, although their evidential roles differ: the terrain surveys describe local landforms, whereas the slope analysis describes the distribution of detections within the imposed mapping constraints. Neither constitutes independent validation of the historical flood boundaries, particularly because low slopes and proximity to channels were already incorporated into the mapping procedure.

The predominance of rice fields and agricultural mosaics in the land-cover overlay indicates that agricultural land accounts for much of the mapped exposure. This overlap identifies land uses associated with the detections but does not establish crop damage or economic loss. Its temporal interpretation also depends on the land-cover product used. The recurrence overlay describes the land cover represented in the 2024 map, rather than reconstructing its distribution throughout 2019–2025. The complementary event-level overlays improve temporal correspondence by using the available classification for each event year, although E12 and E13 also rely on the 2024 product. Cumulative event areas and the area detected at least once consequently represent different aspects of exposure: cumulative areas include repeated detections of the same land, whereas the spatial union counts that land only once.

Agricultural water management introduces an additional uncertainty in these overlays because PRE–POST backscatter changes can reflect river flooding, rice-field preparation, or irrigation. The regional agricultural calendar documents rice sowing and harvesting throughout the year [53]. Monthly rice-stage dynamics have also been documented in the lower Utcubamba basin during 2019–2020 [54]. This context is particularly relevant to the three retained events outside the main wet season: E04 in October 2019, E06 in June 2020, and E08 in November 2021. Documentary evidence differs among these events: E04 is supported by an official river-overflow report [40], E06 appears in the SENAMHI flood-event inventory, and E08 is associated with earthquake-triggered blockage of the Utcubamba River at Aserradero [41]. These records do not establish the mapped flood extent, and the available documentation does not resolve the mechanism of E06. Agricultural classes represented a larger share of cumulative detections outside the wet season than within it (84% versus 64%; Section 3.7). This difference is consistent with a possible contribution from agricultural water management but does not identify or quantify irrigation-related false positives. Date-specific georeferenced records of irrigated parcels were unavailable for a direct assessment. Nevertheless, repeated detections remained concentrated near the confluence in the wet-season subset (Supplementary Table S1), indicating that this spatial pattern was not restricted to the three events outside the main wet season.

The representation of non-flooded conditions is another relevant methodological choice. A comparison of four Sentinel-1 change-detection methods found that a reference accounting for backscatter seasonality produced the best results across the evaluated methods [55]. Here, the PRE timing test examined changes in scene availability and classification thresholds, rather than differences in classification accuracy.

The event catalog also conditions the interpretation of observed recurrence. It was assembled from official records consulted through SINPAD–INDECI and the SENAMHI flood-event inventory [40,41]. This approach provides a documented basis for event selection but makes the analysis dependent on the availability and completeness of those records. Events absent from the consulted sources could not be represented, introducing a potential reporting bias whose magnitude was not assessed. The subsequent quality controls further restricted the analysis to events meeting the temporal and radiometric criteria. The resulting eight-event dataset therefore represents a selected set of documented floods rather than a complete record of inundation during 2019–2025. Consequently, differences in recurrence counts describe repeated detections within that set and cannot be interpreted directly as differences in annual flood probability. Independent hydrometric corroboration of the cataloged events was not possible: the Corral Quemado station monitors the Marañón River, and daily precipitation records were available only for E12 and E13 (Supplementary Table S4). Continuous discharge monitoring on the Utcubamba River, through new or reactivated gauging stations, would allow future studies to corroborate the occurrence and relative magnitude of cataloged events.

Satellite acquisition timing further affects comparisons among events. Limited temporal coverage can miss the maximum flood extent or capture different stages of inundation and recession [21,56]. In the Utcubamba Valley, acquisition dates and scene counts varied among events, so the mapped areas represent flooding detectable within the selected observation windows. The magnitude of this temporal sampling effect was not quantified. Hydroclimatic variability may also contribute to differences among events. ENSO produces spatially variable precipitation responses across Peru [5], and Pacific and tropical Atlantic variability can influence flood characteristics in the Amazon basin [4]. However, the present catalog was not stratified by climate phase. The observed differences therefore cannot be attributed directly to ENSO, given the additional influences of documentary coverage, event selection, and satellite timing.

The close temporal spacing of E12 and E13 requires a further distinction between cataloged events and hydrologically independent episodes. These records were retained separately because they have distinct catalog dates and subsequent SAR observations. Differences in their detected footprints and precipitation context provide additional information (Supplementary Tables S4 and S5), but do not conclusively establish independence or demonstrate that both records belong to a single prolonged episode. The E13 PRE reference preceded the cataloged date of E12 and met the temporal overlap criterion. Nevertheless, shared POST detections may include persistent inundation or moisture, so compliance with that criterion does not resolve the relationship between the two episodes. When detections shared by E12 and E13 were counted once, the area with at least four detections decreased from approximately 633 to 307 ha, although 53% of that area remained within 15 km of the confluence (Supplementary Table S5). Their contribution to the recurrence map is therefore interpreted as detections associated with separate catalog records, with explicit uncertainty concerning their hydrological independence.

The spatial sensitivity analysis showed that detected extent also responds to the restrictions imposed during processing. Within the evaluated ranges, changes in hydrographic buffer distance produced larger area differences than changes in maximum slope. Meanwhile, the narrow range of VH thresholds in the slope scenarios did not imply a constant classified area. Threshold consistency and stability of detected extent thus describe different properties of the results. These tests quantify the influence of the parameters, but do not identify which configuration is most accurate. That determination would require suitable reference data for the areas added or removed and an assessment consistent with the sampling design [51]. The 1000 m buffer and 5° slope limit should therefore be understood as local processing choices. Post-processing can also affect the spatial detail retained in flood maps: filtering intended to reduce speckle has been shown to remove relevant features in small-scale inundation patterns [50]. Sensitivity to smoothing radius, minimum mapping unit, and the elevation limit was not evaluated in the present study, and the suitability of the processing parameters in other settings remains to be assessed. A quantitative comparison with the Copernicus Global Flood Monitoring (GFM) product, which would require harmonizing the acquisitions and the spatial domain evaluated, was not carried out and remains a possible extension of this work.

Together, the event maps, recurrence analysis, land-cover overlays, and local terrain information characterize repeated detections and their agricultural and geomorphological setting within the study area. Their practical contribution is to identify sectors that warrant closer assessment and to support territorial planning with spatial evidence from documented events. This use must remain consistent with what the maps measure: observed recurrence among selected catalog records, rather than annual flood probability or return periods. Likewise, the agricultural overlays describe mapped exposure rather than damage.

Applications requiring flood probabilities, expected losses, or regulatory boundaries would need additional hydrological and vulnerability assessments.

5. Conclusions

The multitemporal analysis of eight retained flood events during 2019–2025 identified a spatial concentration of repeated detections in the Utcubamba Valley. VH yielded the lowest dispersion of Otsu thresholds among the retained events, a property of the selected subset rather than independent evidence of temporal stability, and the highest accuracy point estimates in the E13 reference sample, supporting its selection under the conditions evaluated. The area detected as flooded at least once covered 9842.02 ha, of which 78.72% was detected in one or two events. High and very high observed recurrence accounted for 6.29% and was concentrated near the Utcubamba–Marañón confluence and northern valley meanders. UAV-derived terrain models provided complementary geomorphological context for these patterns.

The predominance of rice fields and agricultural mosaics within the detected areas highlights the relevance of multitemporal flood mapping to agricultural land-use planning. The workflow integrates Sentinel-1 observations, automatic thresholding, observed recurrence, and land-cover information to identify repeatedly detected sectors and characterize their mapped exposure. Recurrence represents detections among the selected cataloged events, while agricultural detections may include changes associated with irrigation or field preparation. Application elsewhere requires local evaluation of the observation windows, topographic and hydrographic constraints, and classification accuracy. Within this scope, the approach provides a practical basis for documenting flood-related spatial patterns and supporting territorial planning in an Andean–Amazonian valley with limited hydrological information.

Supplementary Materials: The following supporting information can be downloaded at https://www.mdpi.com/article/10.3390/rs18213756/s1: Table S1: Observed recurrence and spatial distribution of detections by event group; Table S2: Land-cover composition of cumulative detections by event group; Table S3: Overlap between detections in wet-season and out-of-season events; Table S4: Daily precipitation context for E12 and E13; Table S5: Spatial overlap of E12 and E13 and sensitivity of high observed recurrence to their grouping.

Author Contributions: Conceptualization, W.H.V.-F. and A.S.R.-F.; methodology, W.H.V.-F., A.S.R.-F., J.A.Z.-S. and A.J.M.-M.; software, W.H.V.-F. and S.S.; validation, W.H.V.-F., A.C.-S., A.S.R.-F. and J.A.Z.-S.; formal analysis, W.H.V.-F., A.S.R.-F., J.A.Z.-S., T.B.S.-M. and A.J.M.-M.; investigation, W.H.V.-F., K.M.T.-T., M.R.P.-H., A.J.M.-M., T.B.S.-M. and E.B.; resources, E.B.; data curation, W.H.V.-F. and K.M.T.-T.; writing—original draft preparation, W.H.V.-F.; writing—review and editing, A.S.R.-F., S.S., M.R.P.-H., E.B. and A.C.-S.; visualization, W.H.V.-F.; supervision, E.B.; project administration, E.B.; funding acquisition, E.B. All authors have read and agreed to the published version of the manuscript.

Funding: This research was funded by CONCYTEC through the PROCIENCIA program under the Applied Research Projects 2025-02 competition, Contract No. PE501096734-2025-PROCIENCIA. The APC was funded by the Vice-Rectorate for Research of the Universidad Nacional Toribio Rodríguez de Mendoza de Amazonas (UNTRM).

Data Availability Statement: The datasets generated and analyzed during the current study, including the Sentinel-1 SAR-derived flood extent maps, event selection summary, and processing code, are publicly available in Figshare at https://doi.org/10.6084/m9.figshare.33322791 (accessed on 30 September 2026).

Acknowledgments: The authors sincerely thank the Servicio Nacional de Meteorología e Hidrología del Perú (SENAMHI) for providing precipitation records for the study area, and the Instituto Nacional de Defensa Civil (INDECI) for facilitating access to historical flood-event records through the SINPAD platform.

Conflicts of Interest: The authors declare no conflicts of interest.

References

1. Gasmi, F.; Aly, M.H. A Comprehensive Systematic Review of Contemporary Geospatial Approaches to Flood Hazard and Risk Assessment. *Urban Sci*. **2026**, *10*, 271. [CrossRef]
2. Sun, Y.; Li, X.; Wang, D.; Han, Y.; Qin, Y.; Gong, S.; Qiao, W.; Fu, C. Multi-Source SAR Data-Driven Flood Extent Mapping and Flood Risk Assessment in the Coastal Area of East China: A Case Study of Donghai County, Lianyungang. *Prog*. *Disaster Sci*. **2026**, *31*, 100620. [CrossRef]
3. Klacso, J.; Gogova, L.; Hledik, J. Orienteering with Flood Maps: The Potential Impact of Riverine Floods on Corporate Credit Risk. *Int*. *Rev*. *Financ*. *Anal*. **2026**, *117*, 105223. [CrossRef]
4. Towner, J.; Ficchí, A.; Cloke, H.L.; Bazo, J.; Coughlan De Perez, E.; Stephens, E.M. Influence of ENSO and Tropical Atlantic Climate Variability on Flood Characteristics in the Amazon Basin. *Hydrol*. *Earth Syst*. *Sci*. **2021**, *25*, 3875–3895. [CrossRef]
5. Sulca, J.; Takahashi, K.; Espinoza, J.; Vuille, M.; Lavado-Casimiro, W. Impacts of Different ENSO Flavors and Tropical Pacific Convection Variability (ITCZ, SPCZ) on Austral Summer Rainfall in South America, with a Focus on Peru. *Int*. *J*. *Climatol*. **2018**, *38*, 420–435. [CrossRef]
6. Yglesias-González, M.; Valdés-Velásquez, A.; Hartinger, S.M.; Takahashi, K.; Salvatierra, G.; Velarde, R.; Contreras, A.; Santa María, H.; Romanello, M.; Paz-Soldán, V.; et al. Reflections on the Impact and Response to the Peruvian 2017 Coastal El Niño Event: Looking to the Past to Prepare for the Future. *PLoS ONE* **2023**, *18*, e0290767. [CrossRef]
7. Xu, Y.; Wang, X. Mountainous Urban Development Unintentionally Reshapes Spatial Patterns of Flood Disaster Risk. *Int*. *J*. *Disaster Risk Reduct*. **2026**, *141*, 106206. [CrossRef]
8. Li, J.; Liu, G.; Wang, H.; Guo, J.; Chen, H.; Wang, T. Study on the Interaction Mechanisms of Urban Flood Risk Driving Factors Based on Explainable Machine Learning: A Human-Centered Assessment Framework. *J*. *Clean*. *Prod*. **2026**, *567*, 148656. [CrossRef]
9. Amitrano, D.; Di Martino, G.; Di Simone, A.; Imperatore, P. Flood Detection with SAR: A Review of Techniques and Datasets. *Remote Sens*. **2024**, *16*, 656. [CrossRef]
10. Yu, H.; Wang, R.; Li, P.; Zhang, P. Flood Detection in Polarimetric SAR Data Using Deformable Convolutional Vision Model. *Water* **2023**, *15*, 4202. [CrossRef]
11. Shan, W.; Liu, J.; Guo, Y. Rapid Flood Mapping and Disaster Assessment Based on GEE Platform: Case Study of a Rainstorm from July to August 2024 in Liaoning Province, China. *Water* **2025**, *17*, 2416. [CrossRef]
12. Martinis, S.; Rieke, C. Backscatter Analysis Using Multi-Temporal and Multi-Frequency SAR Data in the Context of Flood Mapping at River Saale, Germany. *Remote Sens*. **2015**, *7*, 7732–7752. [CrossRef]
13. Jean Milien, E.; Girard, P.; da Cunha, C.N. Hydrological Dynamics of Large Tropical Savanna Wetland Through Sentinel-1 SAR Imagery: Pantanal Ramsar Site Case Study. *Water* **2026**, *18*, 778. [CrossRef]
14. van Rutten, P.; Benito Lazaro, I.; Muis, S.; Teklesadik, A.; van den Homberg, M. Flood and Rice Damage Mapping for Tropical Storm Talas in Vietnam Using Sentinel-1 SAR Data. *Remote Sens*. **2025**, *17*, 2171. [CrossRef]
15. Paul, G.; Alam, S.K.A. Integrating Sentinel-1 SAR Data with Google Earth Engine for Enhanced Flood Detection in Lakhimpur District in Assam, India. In *Geospatial Techniques in Climate Change Monitoring and Environmental Mapping*; Elsevier: Amsterdam, The Netherlands, 2026; pp. 297–317.
16. Zhuang, H.; Wang, P.; Hao, M.; Fan, H.; Tan, Z. Flood Inundation Mapping in SAR Images Based on Nonlocal Polarization Combination Features. *J*. *Hydrol*. **2025**, *646*, 132326. [CrossRef]
17. Veedu, J.T.; Reghunadhan, R. Digital Elevation Model and SAR Imagery—A Marriage for Effectual Flood Detection Using Novel Lightweight Ensemble Neural Networks. *Remote Sens*. *Appl*. **2026**, *42*, 102031. [CrossRef]
18. Wang, X.; Dai, K.; Xiang, J.; Deng, J.; Wu, D.; Wen, N.; Liang, R.; Saeed, K. A Novel Dual-Polarization SAR-Based Method for High-Accuracy 768 Km River Mapping in Steep Mountainous Regions. *Int*. *J*. *Appl*. *Earth Obs*. *Geoinf*. **2026**, *147*, 105190. [CrossRef]
19. Guan, H.; Huang, J.; Li, L.; Li, X.; Miao, S.; Su, W.; Ma, Y.; Niu, Q.; Huang, H. Improved Gaussian Mixture Model to Map the Flooded Crops of VV and VH Polarization Data. *Remote Sens*. *Environ*. **2023**, *295*, 113714. [CrossRef]
20. Tazmul Islam, M.; Meng, Q. An Exploratory Study of Sentinel-1 SAR for Rapid Urban Flood Mapping on Google Earth Engine. *Int*. *J*. *Appl*. *Earth Obs*. *Geoinf*. **2022**, *113*, 103002. [CrossRef]
21. Clement, M.A.; Kilsby, C.G.; Moore, P. Multi-Temporal Synthetic Aperture Radar Flood Mapping Using Change Detection. *J*. *Flood Risk Manag*. **2018**, *11*, 152–168. [CrossRef]
22. McCormack, T.; Campanyà, J.; Naughton, O. A Methodology for Mapping Annual Flood Extent Using Multi-Temporal Sentinel-1 Imagery. *Remote Sens*. *Environ*. **2022**, *282*, 113273. [CrossRef]
23. Hieu, N.M.; Trang, T.T.K.; Bac, D.K.; Oanh, V.T.K.; Nga, P.T.P.; Tuan, T.V.; Phin, P.T.; Liem, P.S.; Thu, D.T.T.; Hung, V.K. An Integrated Approach to Assessing the Impacts of Urbanization on Urban Flood Hazards in Hanoi, Vietnam. *Sustainability* **2025**, *17*, 10763. [CrossRef]
24. Nasanlı, O.; R, K.; Tan, N. A Dynamic AHP–GIS Framework for Spatio-Temporal Flood Risk Assessment Incorporating Flood Risk Transfer Index (FRTI). *Sustainability* **2026**, *18*, 5038. [CrossRef]

25. Thapa, N.; Nepali, S.; Shrestha, R.; Sanjel, S. Time Series Flood Mapping Using the Copernicus Dataset in Google Earth Engine of the Mountainous Region. *Data Brief* **2025**, *62*, 112010. [CrossRef]
26. Gintauskas, J.; Bučas, M.; Vaičiūtė, D.; Tiškus, E. Spatiotemporal Patterns of Inundation in the Nemunas River Delta Using Sentinel-1 SAR: Influence of Land Use and Soil Composition. *Hydrology* **2025**, *12*, 245. [CrossRef]
27. Shen, X.; Wang, D.; Mao, K.; Anagnostou, E.; Hong, Y. Inundation Extent Mapping by Synthetic Aperture Radar: A Review. *Remote Sens.* **2019**, *11*, 879. [CrossRef]
28. United Nations General Assembly. *Report of the Open-Ended Intergovernmental Expert Working Group on Indicators and Terminology Relating to Disaster Risk Reduction*; United Nations: New York, NY, USA, 2016; A/71/644.
29. Barboza, E.; Corroto, F.; Salas, R.; Gamarra, Ó.; Ballarín, D.; Ollero, A. Hidrogeomorfología En Áreas Tropicales: Aplicación Del Índice Hidrogeomorfológico (IHG) En El Río Utcubamba (Perú). *Ecol. Apl.* **2017**, *16*, 39–47. [CrossRef]
30. Rojas Briceño, N.; Barboza Castillo, E.; Gamarra Torres, O.; Oliva, M.; Leiva Tafur, D.; Barrena Gurbillón, M.; Corroto, F.; Salas López, R.; Rascón, J. Morphometric Prioritization, Fluvial Classification, and Hydrogeomorphological Quality in High Andean Livestock Micro-Watersheds in Northern Peru. *ISPRS Int. J. Geoinf.* **2020**, *9*, 305. [CrossRef]
31. SENAMHI. *Pronóstico Hidrológico Estacional a Nivel Nacional*; Servicio Nacional de Meteorología e Hidrología del Perú: Lima, Peru, 2026.
32. SENAMHI. *Clima Del Perú*; Servicio Nacional de Meteorología e Hidrología del Perú: Lima, Peru, 2021.
33. Rivera-Fernandez, A.S.; Cotrina-Sanchez, A.; Salas López, R.; Zabaleta-Santisteban, J.A.; Rios, N.; Medina-Medina, A.J.; Tuesta-Trauco, K.M.; Sánchez-Vega, J.A.; Silva-Melendez, T.B.; Oliva-Cruz, M.; et al. Spatiotemporal Land Cover Change and Future Hydrological Impacts Under Climate Scenarios in the Amazonian Andes: A Case Study of the Utcubamba River Basin. *Land* **2025**, *14*, 1234. [CrossRef]
34. CEPLAN. *Amazonas 1 Potencialidades Productivas Desde Un Enfoque Territorial*; Centro Nacional de Planeamiento Estratégico: Lima, Peru, 2025.
35. INEI. *Censos Nacionales 2017: XII de Población, VII de Vivienda y III de Comunidades Indígenas*; Instituto Nacional de Estadística e Informática: Lima, Peru, 2018.
36. European Space Agency (ESA). Copernicus DEM GLO-30: Global Digital Elevation Model. Copernicus DEM 2022. Available online: https://gee-community-catalog.org/projects/glo30/ (accessed on 5 September 2026).
37. Torres, R.; Snoeij, P.; Geudtner, D.; Bibby, D.; Davidson, M.; Attema, E.; Potin, P.; Rommen, B.Ö.; Floury, N.; Brown, M.; et al. GMES Sentinel-1 Mission. *Remote Sens. Environ.* **2012**, *120*, 9–24. [CrossRef]
38. Amer, R. Machine Learning-Driven Rapid Flood Mapping for Tropical Storm Imelda Using Sentinel-1 SAR Imagery. *Remote Sens.* **2025**, *17*, 1869. [CrossRef]
39. Mullissa, A.; Vollrath, A.; Odongo-Braun, C.; Slagter, B.; Balling, J.; Gou, Y.; Gorelick, N.; Reiche, J. Sentinel-1 SAR Backscatter Analysis Ready Data Preparation in Google Earth Engine. *Remote Sens.* **2021**, *13*, 1954. [CrossRef]
40. INDECI. SINPADv2.0—Sistema de Información Nacional Para La Respuesta y Rehabilitación. Available online: https://sinpad2.indeci.gob.pe/sinpad2/faces/public/portal.html (accessed on 3 July 2026).
41. Sardon, H.; Lavado-Casimiro, W.Y.; Felipe, O. *Inventario de Datos de Eventos de Inundaciones Del Perú*; Servicio Nacional de Meteorología e Hidrología del Perú: Lima, Peru, 2022.
42. Bindschadler, R.A.; Scambos, T.A.; Choi, H.; Haran, T.M. Ice Sheet Change Detection by Satellite Image Differencing. *Remote Sens. Environ.* **2010**, *114*, 1353–1362. [CrossRef]
43. Minu, S.; Shetty, A. A Comparative Study of Image Change Detection Algorithms in MATLAB. *Aquat. Procedia* **2015**, *4*, 1366–1373. [CrossRef]
44. Conde, F.C.; De Mata Muñoz, M. Flood Monitoring Based on the Study of Sentinel-1 SAR Images: The Ebro River Case Study. *Water* **2019**, *11*, 2454. [CrossRef]
45. Breña Aliaga, J.C.; Vidal, J.; Felipe, O.; Bourrel, L.; Rau, P.; Lavado-Casimiro, W. Estimation of Flood Thresholds for Hydrological Warning Purposes Using Sentinel-1 SAR Imagery-Based Modeling in the Tumbes River Basin (PERU). *Remote Sens.* **2026**, *18*, 1493. [CrossRef]
46. Nhangumbe, M.; Nascetti, A.; Ban, Y. Multi-Temporal Sentinel-1 SAR and Sentinel-2 MSI Data for Flood Mapping and Damage Assessment in Mozambique. *ISPRS Int. J. Geo-Inf.* **2023**, *12*, 53. [CrossRef]
47. Wilson, E.B. Probable Inference, the Law of Succession, and Statistical Inference. *J. Am. Stat. Assoc.* **1927**, *22*, 209–212. [CrossRef]
48. Bangira, T.; Iannini, L.; Menenti, M.; van Niekerk, A.; Vekerdy, Z. Flood Extent Mapping in the Caprivi Floodplain Using Sentinel-1 Time Series. *IEEE J. Sel. Top. Appl. Earth Obs. Remote Sens.* **2021**, *14*, 5667–5683. [CrossRef]
49. Tran, K.H.; Menenti, M.; Jia, L. Surface Water Mapping and Flood Monitoring in the Mekong Delta Using Sentinel-1 SAR Time Series and Otsu Threshold. *Remote Sens.* **2022**, *14*, 5721. [CrossRef]
50. Roth, F.; Tupas, M.E.; Navacchi, C.; Zhao, J.; Wagner, W.; Bauer-Marschallinger, B. Evaluating the Robustness of Bayesian Flood Mapping with Sentinel-1 Data: A Multi-Event Validation Study. *Sci. Remote Sens.* **2025**, *11*, 100210. [CrossRef]

51. Olofsson, P.; Foody, G.M.; Herold, M.; Stehman, S.V.; Woodcock, C.E.; Wulder, M.A. Good Practices for Estimating Area and Assessing Accuracy of Land Change. *Remote Sens. Environ.* **2014**, *148*, 42–57. [CrossRef]
52. Stehman, S.V.; Foody, G.M. Key Issues in Rigorous Accuracy Assessment of Land Cover Products. *Remote Sens. Environ.* **2019**, *231*, 111199. [CrossRef]
53. Ministerio de Desarrollo Agrario y Riego. *Observatorio de Siembras y Perspectivas de La Producción: Arroz*; Ministerio de Desarrollo Agrario y Riego: Lima, Peru, 2023.
54. Medina Medina, A.J.; Salas López, R.; Zabaleta Santisteban, J.A.; Tuesta Trauco, K.M.; Turpo Cayo, E.Y.; Huaman Haro, N.; Oliva Cruz, M.; Gómez Fernández, D. An Analysis of the Rice-Cultivation Dynamics in the Lower Utcubamba River Basin Using SAR and Optical Imagery in Google Earth Engine (GEE). *Agronomy* **2024**, *14*, 557. [CrossRef]
55. Tupas, M.E.; Roth, F.; Bauer-Marschallinger, B.; Wagner, W. An Intercomparison of Sentinel-1 Based Change Detection Algorithms for Flood Mapping. *Remote Sens.* **2023**, *15*, 1200. [CrossRef]
56. Roth, F.; Bauer-Marschallinger, B.; Tupas, M.E.; Reimer, C.; Salamon, P.; Wagner, W. Sentinel-1-Based Analysis of the Severe Flood over Pakistan 2022. *Nat. Hazards Earth Syst. Sci.* **2023**, *23*, 3305–3317. [CrossRef]

Disclaimer/Publisher's Note: The statements, opinions and data contained in all publications are solely those of the individual author(s) and contributor(s) and not of MDPI and/or the editor(s). MDPI and/or the editor(s) disclaim responsibility for any injury to people or property resulting from any ideas, methods, instructions or products referred to in the content.